JOURNAL OF THERMOPHYSICS AND HEAT TRANSFER
Vol. 19, No. 1, January–March 2005

Hydrodynamic Study of High-Speed Flow and Heat Transfer Through a Microchannel

Reni Raju* and Subrata Roy†
Kettering University, Flint, Michigan 48504

Fluid flow and heat-transfer characteristics in microchannels are investigated using a finite element based hydrodynamic model with first-order slip/jump boundary conditions. Helium and nitrogen are utilized as working fluid, and the Knudsen-number ranges from slip to transition regime. Results for high-speed compressible gas flow for two separate cases for a microchannel with rough surface and an aspect ratio of five have been compared with published direct-simulation Monte Carlo results. Despite some noticeable differences, the hydrodynamic model compares favorably in predicting the flow structure and heat-transfer characteristics for high-speed microflows.

Nomenclature

C_p = specific heat at constant pressure
H = height of the channel
Kn = Knudsen number
k = thermal conductivity
L = length of the channel
Ma = Mach number
P = gas pressure
Pr = Prandtl number
R = reduced gas constant
T = temperature
t = time
u = gas velocity in x direction
v = gas velocity in y direction
γ = specific heat ratio
Λ = reference length
λ = mean free path of the fluid
μ = coefficient of viscosity
ρ = gas density
σ_T = thermal-momentum coefficient
σ_v = tangential-momentum coefficient

Subscripts

g = gas properties
w = wall properties
0 = reference quantity

Introduction

ADVANCEMENTS in micromachining techniques and potential areas of application have led to the significant development of the micro- and mesoscale systems. Specifically, developments of microheaters, micro-heat exchangers/sinks for electronic cooling, microspacecraft controls, and similar devices emphasize the need to comprehend the heat-transfer characteristics of fluids in microchannels. Typically, mechanical devices with dimensions below 1 mm up to 1 μm are called microelectromechanical systems. At these scales however the dimensions of the system itself become comparable to the mean free path of the particles inside the system. For liquid, this in turn tends to make the flow granular in nature, whereas for gases the flow becomes rarefied. Because fundamentally the flow behavior and heat-transfer characteristics in microdevices are different than in macrosystems, it is necessary to understand and analyze the physics/laws governing these systems. Studies reflect that the standard continuum approach of considering the bulk of the fluid with no-slip wall conditions can no longer predict the momentum and heat transfer accurately in microdevices. As the flow becomes molecular, a number of other parameters start playing a significant role in governing the heat and momentum transfer. These include the surface forces, roughness, rarefaction, viscous forces, and thermal creep,[1] which are not dominant in macroscopic flows.

The degree of rarefaction and applicability of the continuum model is determined by the local value of the Knudsen number and is defined as $Kn = \lambda/\Lambda = 16\mu/5\rho\sqrt{(2\pi RT)}$ (based on Chapman–Enskog result). Depending on the value of Knudsen number, the flow can be divided into four categories.[2] For $Kn < 0.001$, the flow can be assumed to be a continuum such is the case for macroscopic flows, whereas for $Kn > 10$ it becomes free molecular. However, in the region of 0.001–10 the flow is neither sufficiently continuum nor completely molecular. Thus, it can be further divided into two separate regions, slip-flow regime for $0.001 < Kn < 0.1$ and transition regime for $0.1 < Kn < 10$.

It has been found that the Navier–Stokes equations with first-order velocity-slip[3] and temperature-jump[4] boundary correction work well for the slip flow regime ($0.001 < Kn < 0.1$). However, with the increasing Knudsen number the bulk nature of the fluid properties reduces, and the flow becomes molecular. Because of the rarefaction of the fluids, higher-order boundary conditions are suggested[1] when the flow enters the transition regime ($0.1 < Kn < 10$). The general computational tools for this region are Boltzmann equation methods, statistical methods, and Burnett equation with slip boundary conditions.[5]

Over the past two decades several experimental investigations have been carried out to determine the heat-transfer characteristics in microchannels. In one of the earliest experiments, Wu and Little[6] have measured heat transfer in fine channels. Pfahler et al.[7] have measured friction coefficients for laminar fluids in the microchannels. Choi et al.[8] have studied heat transfer in 3–81 μm long microtubes. Heat-transfer performance and cooling characteristics of subcooled liquid through 0.7-mm-deep microchannels have been measured by Peng et al.[9] Adams et al.[10] have tried to enhance heat transfer of forced liquid convection using dissolved noncondensables while Mala et al.[11] investigated the effect of electric double layer in a flow between parallel plates.

The popular methods for analyzing the heat-transfer characteristics of gases in microchannels include the particulate method of Boltzmann equation, direct-simulation Monte Carlo[12] (DSMC) and

Presented as Paper 4051-2003 at the AIAA 36th Thermophysics Conference, Orlando, FL, 23–26 June 2003; received 22 April 2004; revision received 6 July 2004; accepted for publication 7 July 2004.

*Graduate Student, Computational Plasma Dynamics Laboratory, Department of Mechanical Engineering; currently Graduate Research Assistant, George Washington University; reni@gwu.edu. Student Member AIAA.

†Associate Professor, Computational Plasma Dynamics Laboratory, Department of Mechanical Engineering; sroy@kettering.edu. Associate Fellow AIAA.

Burnett equation models[13,14] because they give a better resolution for gas-to-surface interactions. Several investigators have used the DSMC approach especially in case of high-speed flows, where the Knudsen number is relatively high.[5,15–17] However the major drawback of this approach is that it is prohibitively expensive because of the high computation cost and time requirement[1,15,18] to achieve any practical resolution. The primary aim of microfluidics is to know the averaged quantities of the various parameters rather than the molecular information to predict the flow behavior. A more feasible approach would be considering bulk approach for the fluid flow while accommodating the different effects encountered in microfluidics like wall slip, compressibility, rarefaction and thermal creep, thus yielding a closer approximation to the overall behavior of the flow in the domain at lower cost and practical turnaround time.

A two-dimensional hydrodynamic model based on the finite element method has been developed at Computational Plasma Dynamics Laboratory for investigating micro- and nanoscale flows.[19–21] The first-order slip/jump boundary conditions utilized in this model have predicted subsonic gas flow through microgeometries[19,20] and benchmarked both experimental[22] and numerical[23] results for microchannels and nanopores.[20] As a complement to our recent publications,[19–21] this paper aims to explore the applicability of hydrodynamic model to investigate heat-transfer characteristics of high-speed compressible flows through microchannels having inlet Knudsen numbers of 0.062 and 0.14. The study is restricted to the gas flows. Because of unavailability of experimental data for high-speed microflows through bounded volumes, the computed results are compared with reported DSMC results.[15,16] To our knowledge, successful implementation of first-order slip boundary to hypersonic microscale flow has not been reported earlier.

Problem Description

The two-dimensional microchannel model shown in Fig. 1 is an extension of the experimental setup of Pong et al.[22] used to study Poiseuille flow through long microchannels. The end effects have been neglected for the two-dimensional analysis. The channel geometry has been modified by Oh et al.[15] for working fluid helium to an aspect ratio L/H of five, in order to obtain hypersonic flow conditions. The value of inlet Knudsen number is 0.14 for this case.

Table 1 Model dimensions and flow parameters

	Case I	Case II
Fluid	Helium	Nitrogen
L, μm	6.0	6.0
H, μm	1.2	1.2
B, μm	1.0	0.6
Kn	0.14	0.062
T_0, K	298	300
T_w, K	298	323
Ma_0	5.0	4.15
P_0, Pa	1.01×10^5	1.01×10^5
R, J/kg · K	2076.9	296.8
C_p, J/kg · K	5192.6	1039.0
μ, N-s/m^2	2.066×10^{-5}	1.85×10^{-5}
k, W/k · m	0.152	0.0259
Υ	1.667	1.40

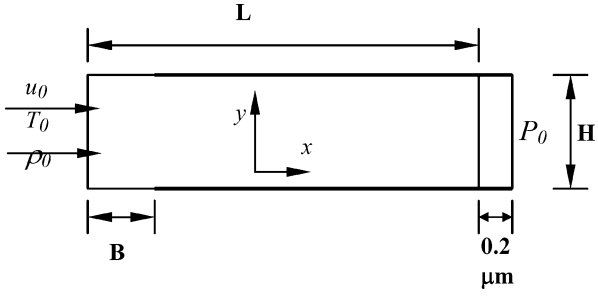

Fig. 1 Schematic of microchannel geometry.[15]

The second case presented by Liou and Fang[16] is similar to the first in terms of dimensions. However the working fluid is nitrogen for this case giving a lower inlet Knudsen number of 0.062. The microchannel dimensions and flow parameters are listed in the Table 1. The flow is simulated at near atmospheric conditions. A freestream region ***B*** is specified near the inlet section of the microchannel where the free gas flow takes place. The boundary conditions remain the same for the two cases.

Governing Equations

The standard two-dimensional, time-dependent, compressible Navier–Stokes (NS) form is used to analyze the gas flow through microchannels:

Conservation of mass:

$$\frac{\partial \rho}{\partial t} + \frac{\partial \rho u}{\partial x} + \frac{\partial \rho v}{\partial y} = 0 \tag{1}$$

Conservation of x momentum:

$$\frac{\partial \rho u}{\partial t} + u\frac{\partial \rho u}{\partial x} + v\frac{\partial \rho u}{\partial y} + \frac{\partial P}{\partial x} - \mu\left[\frac{\partial^2 u}{\partial x^2} + \frac{\partial^2 u}{\partial y^2} + \frac{1}{3}\left(\frac{\partial^2 u}{\partial x^2} + \frac{\partial^2 v}{\partial x \partial y}\right)\right] = 0 \tag{2}$$

Conservation of y momentum:

$$\frac{\partial \rho v}{\partial t} + u\frac{\partial \rho v}{\partial x} + v\frac{\partial \rho v}{\partial y} + \frac{\partial P}{\partial y} - \mu\left[\frac{\partial^2 v}{\partial x^2} + \frac{\partial^2 v}{\partial y^2} + \frac{1}{3}\left(\frac{\partial^2 v}{\partial y^2} + \frac{\partial^2 u}{\partial x \partial y}\right)\right] = 0 \tag{3}$$

Conservation of energy:

$$\rho C_p \frac{\mathrm{D}T}{\mathrm{D}t} - \frac{\mathrm{D}P}{\mathrm{D}t} - \frac{\partial}{\partial x}\left(k\frac{\partial T}{\partial x}\right) - \frac{\partial}{\partial y}\left(k\frac{\partial T}{\partial y}\right) - \mu\left[2\left(\frac{\partial u}{\partial x}\right)^2 + 2\left(\frac{\partial v}{\partial y}\right)^2 + \left(\frac{\partial v}{\partial x} + \frac{\partial u}{\partial y}\right)^2 - \frac{2}{3}\left(\frac{\partial u}{\partial x} + \frac{\partial v}{\partial y}\right)^2\right] = 0 \tag{4}$$

The pressure is defined using the perfect gas law,

$$P = \rho R T \tag{5}$$

Realistically, the viscosity is a function of temperature (for example, see Fig. A1 of Ref. 12). However, we assumed constant molecular viscosity for simplicity. The bulk viscosity assumption is standard with no modification to Stokes hypothesis. The no-slip wall condition is defined as having all components of the velocity vanish at the solid wall. However, as the macroscopic length scale becomes comparable to the fluid mean free path this description becomes vague, and the walls "move". At this stage, streaming velocity at the wall can be described comprising the streaming velocity of incident particles and that of the scattered particles. Maxwell[3] derived slip relations for dilute, monoatomic gases, which have been implemented in the momentum equation,

$$u_g - u_w = \frac{2 - \sigma_V}{\sigma_V}\lambda\left(\frac{\partial u}{\partial y}\right)_w + \frac{3}{4}\frac{\mu}{\rho T_g}\left(\frac{\partial T}{\partial x}\right)_w \tag{6a}$$

Equation (6a) can be modified to the following form using the definition of the Knudsen number:

$$-\mu\left(\frac{\partial u}{\partial y}\right)_w = \frac{5\rho\sigma_V\sqrt{2\pi RT}}{16(2 - \sigma_V)}\left[u_w - u_g + \frac{3}{4}\frac{\mu}{\rho T_g}\left(\frac{\partial T}{\partial x}\right)_w\right] \tag{6b}$$

Corresponding temperature-jump relation for the energy equation was derived by von Smoluchowski[4] as

$$T_g - T_w = \frac{2 - \sigma_T}{\sigma_T}\left[\frac{2\gamma}{\gamma + 1}\right]\frac{\lambda}{Pr}\left(\frac{\partial T}{\partial y}\right)_w \tag{7a}$$

Equation (7a) can also be modified similarly,

$$-k\left(\frac{\partial T}{\partial y}\right)_w = \frac{\sigma_T\sqrt{2\pi RT}}{2-\sigma_T}\left[\frac{\gamma+1}{2\gamma}\right]\frac{5\rho C_p}{16}(T_w - T_g) \qquad (7b)$$

In Eqs. (6) and (7), u_g and T_g are the velocity and temperature of the gas adjacent to the wall, while u_w and T_w are the velocity and temperature at the wall. The tangential-momentum accommodation coefficient σ_V and the thermal accommodation coefficient σ_T at the walls indicate the molecular fraction reflected diffusively from the walls. The second term in Eq. (6a) is known as thermal creep, which generates slip velocity in the direction opposite to the increasing temperature.

Traditionally, the first-order equations (6) and (7) are applied as long as $Kn < 0.1$. Karniadakis and Beskok[1] have presented a higher-order slip boundary condition, which is second-order accurate, for predicting flow accurately for higher Knudsen number in the transition regime. It has been suggested that Maxwell's first-order boundary condition breaks down near $Kn = 0.15$ (Refs. 24 and 25). It has also been suggested that the higher-order slip boundary conditions might actually deviate from the actual solution more than the first-order Maxwell's wall-slip conditions.[3] However, recently it has been shown[26] that for silica pores of radius 1.919 nm with diffusely reflecting walls the viscous flow is dominant at high density and a significant degree of slip controls the flow at low densities. The analysis also showed that for this confined cylindrical geometry at low densities (<4 nm^{-3}) the transport properties of single-component subcritical Lennard–Jones flow could be explained by hydrodynamic mechanisms alone. The constancy of the friction coefficient at the nanopore wall is noted[26,27] as an indicator of the dominance of slip flow. Thus, contrary to the notion of limitation of hydrodynamic model, tangential momentum accommodation coefficient (TMAC) of unity should be able to successfully resolve the Knudsen flow solution, as was shown in Ref. 27. This is a well-understood result. However, Roy et al.[20] have successfully utilized the first-order boundary condition for higher Knudsen numbers of up to 7.36. Because of these reasons, we would restrict slip to first-order conditions (6) and (7).

Numerical Method

The system of Eqs. (1–5) can be represented in more concise form as

$$L(\boldsymbol{q}) = \frac{\partial \boldsymbol{q}}{\partial t} + \frac{\partial\left(\boldsymbol{f}_j - \boldsymbol{f}_j^v\right)}{\partial x_j} - s = 0, \qquad 1 \le j \le 2 \qquad (8a)$$

$$\boldsymbol{q} = \begin{pmatrix} \rho \\ \rho u_i \\ \rho C_p T + P \\ 0 \end{pmatrix}, \qquad \boldsymbol{f}_j = \begin{pmatrix} \rho u_j \\ u_j \rho u_i + P\delta_{ij} \\ u_j(\rho C_p T + P) \\ 0 \end{pmatrix}$$

$$\boldsymbol{f}_j^v = \begin{pmatrix} 0 \\ \tau'_{ij} \\ k\dfrac{\partial T}{\partial x_j} + \tau'_{ij}u_j \\ 0 \end{pmatrix}, \qquad s = \begin{pmatrix} 0 \\ 0 \\ 0 \\ P - \rho RT \end{pmatrix} \qquad 1 \le i \le 2 \qquad (8b)$$

where $\boldsymbol{q}$ is the state variable, $\boldsymbol{f}$ is the kinetic flux vector, $\boldsymbol{f}^v$ the dissipative flux vector, and s is the source term; and

$$\tau'_{ij} = \mu\left(\frac{\partial u_j}{\partial x_j} + \frac{\partial u_j}{\partial x_i}\right) + \delta_{ij}\lambda\frac{\partial u_k}{\partial x_k}, \qquad 1 \le i, j, k \le 2$$

The difficulty involved in achieving a steady-state solution for Eqs. (8a) and (8b) is directly caused by selection of initial conditions. The conventional method of achieving a steady-state solution is to use the time term as a relaxation parameter in the equation system and run the problem until the transient features die down. Here we utilize an artificial diffusion term as an initial condition generator to obtain a final steady-state solution.

Equation (8) can be modified in the following steady-state form:

$$L(\boldsymbol{q}) = \frac{\partial\left(\boldsymbol{f}_j - \boldsymbol{f}_j^v\right)}{\partial x_j} - \beta\frac{\partial^2 \tilde{\boldsymbol{q}}}{\partial x_j^2} - s = 0, \qquad 1 \le i, j \le 2 \qquad (9)$$

where $\tilde{\boldsymbol{q}}^T = (0, u_i, T, 0)$ and β is a diffusion perturbation parameter that can be varied separately for each state variable. As $\beta \to 0$, Eq. (9) reverts back to steady-state form of Eq. (8). Initially β is set to a sufficiently high value so as to generate a diffused but stable convergence to steady-state solution. Progressive reduction of β is carried out until the final steady-state solution with $\beta \to 0$ is achieved. This procedure is analogous to using the transient relaxation.

Using any admissible test function w, the variational integral yields the weak statement (WS) for Eq. (9). Thereafter, the domain Ω and integrated variables $\boldsymbol{q}$ are spatially discretised (Ω_e and $\boldsymbol{Q}$) using Lagrange basis functions N_k complete to the degree k.

$$WS = \int_\Omega w L(\boldsymbol{q})\,\mathrm{d}\Omega = 0, \qquad \Rightarrow WS^h = S_e\left[\int_{\Omega_e} N_k L_e(\boldsymbol{Q})\,\mathrm{d}\tau\right] \equiv 0 \qquad (10a)$$

$$WS^h = S_e\left[\int_{\Omega_e} N_k(-s)\,\mathrm{d}\tau - \int_{\Omega_e}\frac{\partial N_k}{\partial x_j}\left(\boldsymbol{f}_j - \boldsymbol{f}_j^v\right)_e \mathrm{d}\tau + \int_{\partial\Omega_e\cap\partial\Omega^h} N_k\left(\boldsymbol{f}_j - \boldsymbol{f}_j^v\right)_e \hat{n}_j\,\mathrm{d}\sigma\right] \qquad (10b)$$

In Eq. (10), the superscript h denotes discretization and S_e symbolizes the assembly operator carrying local (element e) matrix coefficients into the global arrays. The weak statement naturally yields the surface integrals via application of Green–Gauss theorem in Eq. (10), which contains the unknown boundary fluxes wherever Dirichlet (fixed) boundary conditions are enforced. The zero gradient boundary conditions are automatically enforced via removal of the surface integral. For the slip flow boundary, appropriate surface integrals are replaced by incorporating Eqs. (6b) and (7b) into the momentum and energy equations. Independent of the physical dimension of Ω, and for general forms of the flux vectors, the semidiscretized weak statement of Eq. (10) always yields an ordinary-differential-equation (ODE) system. The terminal ODE is then solved using a Newton–Raphson iterative scheme.

The computational channel geometry is discretized using two-dimensional nonoverlapping nine-noded biquadratic finite elements. The continuity and equation of state are solved for density and pressure respectively using the four corner nodes of the element. For velocity and temperature calculations, all nine nodes of the biquadratic element are used.

The inlet boundary conditions are fixed for velocity u_0 (based on Mach number), temperature T_0, and the density ρ_0 (based on corresponding inlet pressure P_0) as listed in Table 1. The wall temperatures for both the top and bottom surfaces are set to be T_w. The velocity flux is $\partial u/\partial x = 0$ at the outlet, and the y component of the velocity $v = 0$ is specified at the inlet. A backpressure equal to the inlet boundary pressure P_0 is specified at the outlet. The drawback faced for this problem is that outflow boundary conditions could not be replicated because the exact location of the outlet pressure is not clear in any of the references.[15,16] As a result, we specify a backpressure $P_0 = 1.01 \times 10^5$ Pa, 0.2 μm downstream from the exit.

Near the entrance at the wall boundary for the length $\boldsymbol{B}$ (lighter wall), the accommodation coefficients are specified as $\sigma_V = \sigma_T = 0.0$, implying a specular reflection where only the tangential component of velocity of the impinging molecules is conserved; this is the freestream region. In the rest of the domain (darkened wall), the gas-to-wall interactions are set

with $\sigma_V = \sigma_T = 1.0$, implying the gas molecules undergo a complete change in momentum after collision.

Results and Discussions

A single computational grid consisting of 560 finite elements and 3485 nodes was used for both cases. To keep the consistency with the numerical report, the length in the x direction is considered for the length mentioned in Table 1 ignoring the extra length of 0.2 μm for both the cases. Henceforth, we would refer to the study of inlet Knudsen number of 0.14 as case I and that of 0.062 as case II.

The streaming velocity contours for case I (helium) and case II (nitrogen) are shown in Fig. 2. The U velocity remains constant in the "lighter" region and drops down further downstream, (Fig. 2a). Shock waves are seen near both the free stream region and the exit. Because the Knudsen number is high in this case (transitional), a less amount of oblique shock is present, which is prominent on the walls near downstream region. The trend is similar for two cases with helium showing the presence of stronger shock. Figure 3 plots the pressure contours for cases I and II. For helium, shock waves stemming from the leading edges and the exit meet at $x/H = 3.2$ (Fig. 3a). The effect of backpressure is minimal for case II (Figs. 2b and 3b), where nitrogen is used as working fluid. Clearly, the fluidity of helium makes it more interesting with shock interactions with the wall layer. A sharp density rise follows the pressure rise.

Because no experimental data are available for these cases, the first-order Navier–Stokes solution is compared with reported DSMC results[15] for $Kn = 0.14$. However, the centerline profiles are not available for comparison for $Kn = 0.062$. The centerline section of the channel is plotted showing the U velocity and pressure in the streamwise direction. The presence of backpressure plays a dominant role in determining the solution characteristic. Figure 4 compares the hydrodynamic solution of U velocity and pressure distribution at the channel centerline with the DSMC results.[15] Comparison shows a steady drop in downstream velocity for DSMC indicating presence of higher diffusion. A similar trend is seen for pressure (Figs. 4b), reflecting a steady rise. Contrarily, the hydrodynamic solutions captures a sharp shock around $x/H = 3.2$. Note that the inlet Mach number for case II is 5.0.

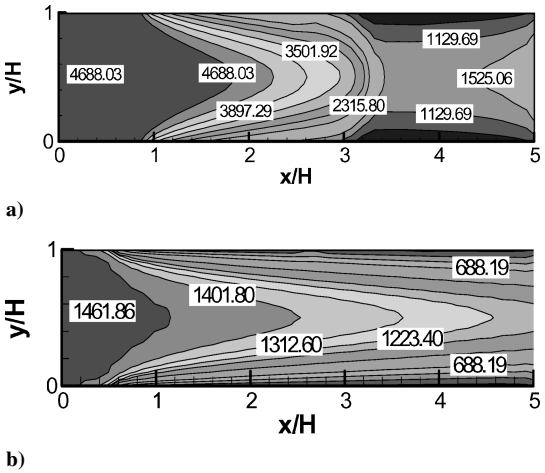

Fig. 2 U-velocity contours for a) $Kn = 0.14$ and b) $Kn = 0.062$.

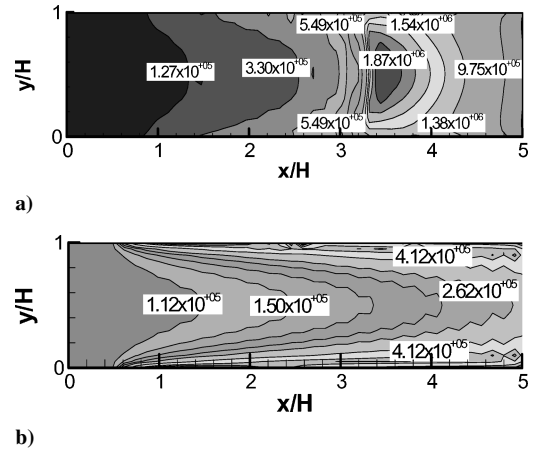

Fig. 3 Computed pressure contours for a) $Kn = 0.14$ and b) $Kn = 0.062$.

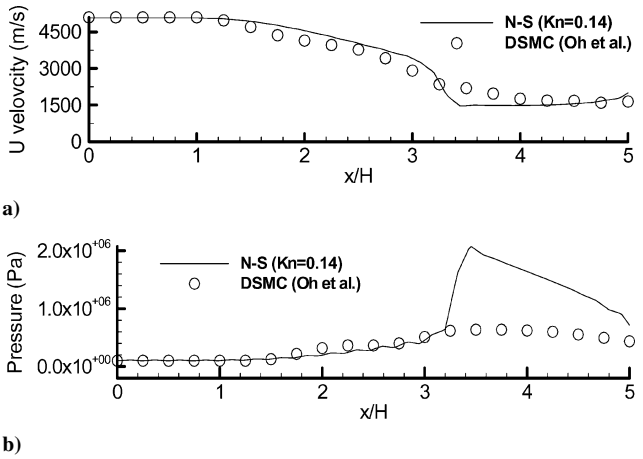

Fig. 4 Comparison of centerline distribution of NS solutions for $Kn = 0.14$ with available DSMC results[15] for a) u velocity and b) pressure.

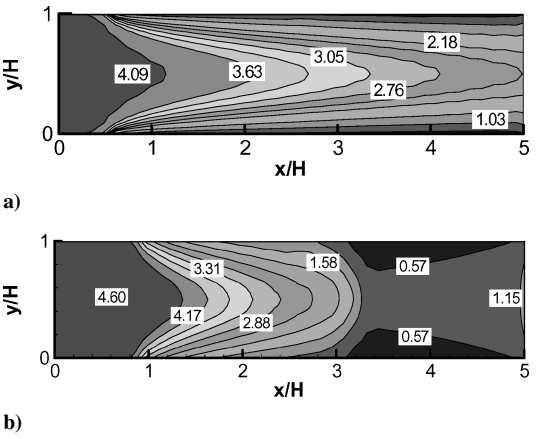

Fig. 5 Mach-number contours for a) $Kn = 0.062$ and b) $Kn = 0.14$.

The Mach-number contours for case II with inlet $Kn = 0.062$ show that the shock emerging from the walls moves towards the center of the channel causing a distortion just ahead of the freestream section. The drop in the Mach number is smooth along the channel as is seen in Fig. 5a. However, for case I with the $Kn = 0.14$ the contours in Fig. 5b plot a relatively sharper drop in velocity. This shows the prevailing viscous effects in the higher Knudsen-number cases.

Figure 6 plots the solution prediction near the wall along the streamwise direction to indicate the slip effects for case I with $Kn = 0.14$. The U velocity near the wall varies between 5000 to 1000 m/s with Mach numbers ranging from 5.0 to nearly 1.0 as a result of the presence of velocity slip and temperature jump. The dominance of the shock caused by the backpressure is also visible in the pressure solution (Fig. 6b). The shock emanating from the walls is the highest near $x/H = 3.2$. Specifically for pressure and density the values beyond the shock are much higher as compared to DSMC predictions.

The temperature contours for the two cases are shown in Fig. 7. Because of shock, the thermal boundary is not completely developed for $Kn = 0.062$. The rise in the temperature is seen the downstream region near the exit (Fig. 7a) at nearly $x/H = 4.2$. This temperature jump is documented upstream for $Kn = 0.14$ at nearly $x/H = 3.4$ as a result of the increase in thermal boundary layer as shown in Fig. 7b.

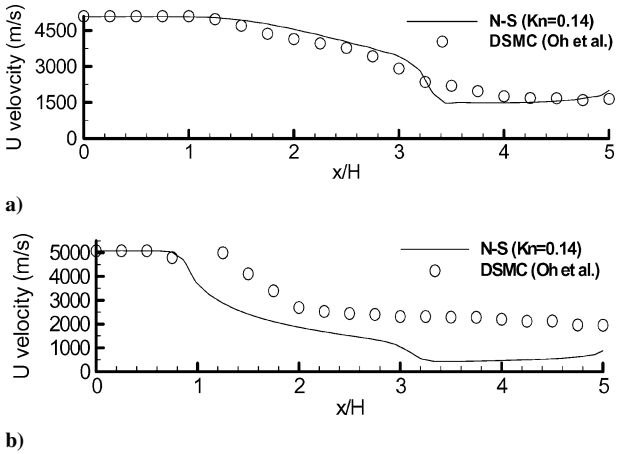

Fig. 6 Comparison of streamwise velocity distribution of NS solutions for $Kn = 0.14$ with available DSMC results[15] at the a) centerline ($y = 0.5$) and b) wall ($y \sim 0$).

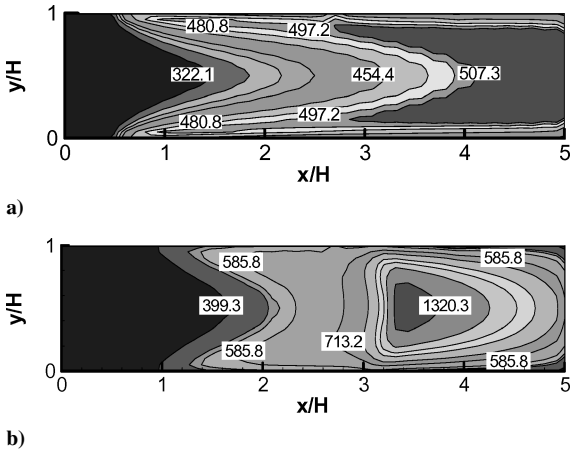

Fig. 7 Temperature contours for a) $Kn = 0.062$ and b) $Kn = 0.14$.

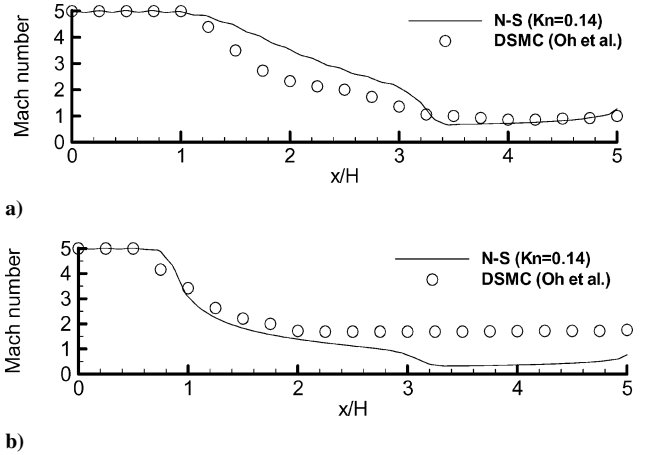

Fig. 8 Comparison of a) centerline ($y = 0.5$) and b) near wall ($y \sim 0$), Mach-number distribution of both NS solutions with available DSMC results[15] for $Kn = 0.14$.

The Mach-number distribution along the centerline and near-wall section of the flow in the streamwise direction is plotted for both of the cases in Figs. 8a and 8b. These results are compared with the reported DSMC solution[15] for $Kn = 0.14$. The centerline Mach number for $Kn = 0.14$ shows a good comparison in the upstream and downstream region with DSMC results. In the midregion, the observed deviation could be caused by the difference in the specification of the location of backpressure as described before. The near-wall ($y \sim 0$) distribution in Fig. 8b also shows a similar comparison with even an exaggerated effect of the backpressure. These findings are consistent with reported Burnett equations model,[14] where the Mach number near the wall matches pretty well with the DSMC solution[15] although in both cases strangely the centerline Mach number is smaller than that near the wall. The computed distribution along the wall (plotted in solid line) is found to be much lower.

Figure 9 compares the centerline and near-wall Mach-number distribution for $Kn = 0.062$. The plotted solution in Fig. 9a shows a smoother drop in the Mach number along the channel centerline as

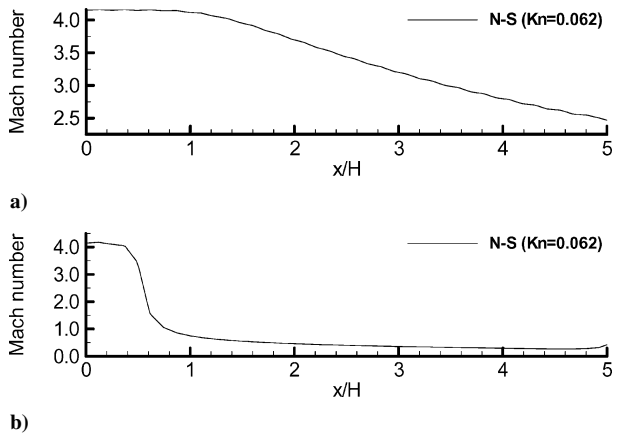

Fig. 9 Mach-number distribution of $Kn = 0.062$ case a) at the centerline ($y = 0.5$) and b) near the wall ($y \sim 0$).

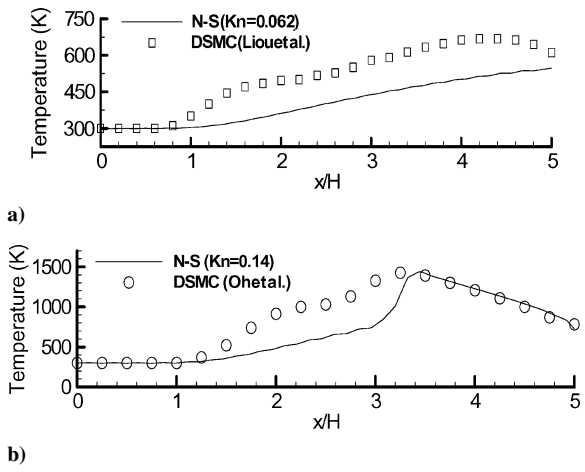

Fig. 10 Comparison of centerline distribution ($y = 0.5$) of temperature compared with the available DSMC results for a) $Kn = 0.062$ (Ref. 16) and b) $Kn = 0.14$ (Ref. 15).

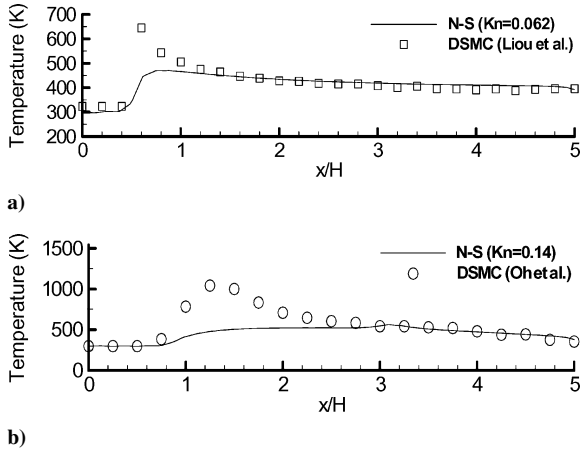

Fig. 11 Comparison of near-wall ($y \sim 0$) distribution of temperature compared with the available DSMC results for a) $Kn = 0.062$ and b) $Kn = 0.14$.

compared to the $Kn = 0.14$ (Fig. 9a). The solution near the walls of the microchannel plotted in Fig. 9b shows that Mach number undergoes a drop immediately after the freestream region and thereafter nearly remains steady. Because no such data at this Knudsen number are not reported elsewhere, there is no means for direct comparison with the literature.

The centerline distribution of temperature for the two cases has been compared in Figs. 10a and 10b. For $Kn = 0.062$, the temperature distributions are similar with a maximum difference of 100 K in the peak value prediction. For $Kn = 0.14$, temperature profiles match in upstream and downstream region like the Mach number. The peak for the temperature matches closely with the referred data. However, compared to the DSMC result, the shock is sharper in the hydrodynamic solution.

Figure 11a shows the near-wall temperature distribution for $Kn = 0.062$, where the peak values of the NS simulation differ from the DSMC results at the end of freestream region; however, for the rest of the domain the values match closely. The solution plotted in Fig. 11b for $Kn = 0.14$ shows that the temperature near the walls remains below 600 K at all places. Deviation from published DSMC results is observed in the region from $x/H = 0.8$ to 2.2. However similar deviation in temperature distribution was also documented for a low (0.07) Knudsen number.[14]

Figure 12 shows comparison of the velocities for five planes in the crosswise direction for $Kn = 0.14$ and 0.062. Sections have been taken at $x/H = 0.8$, 1.0, 2.0, 3.0, 4.0 locations. For $x/H = 0.8$, the Mach number near the center remains the freestream value. A similar trend is shown for $Kn = 0.062$. The drop along the channel is

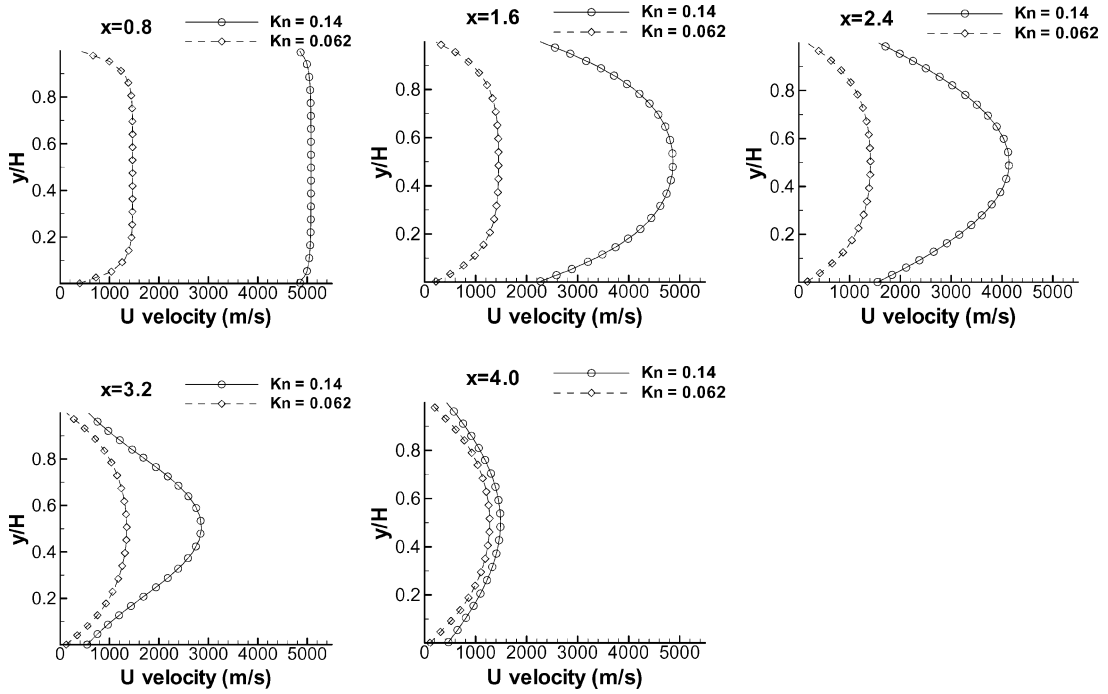

Fig. 12 U velocity distribution along the *y* direction for different streamwise cross sections along the channel for $Kn = 0.14$ and 0.62.

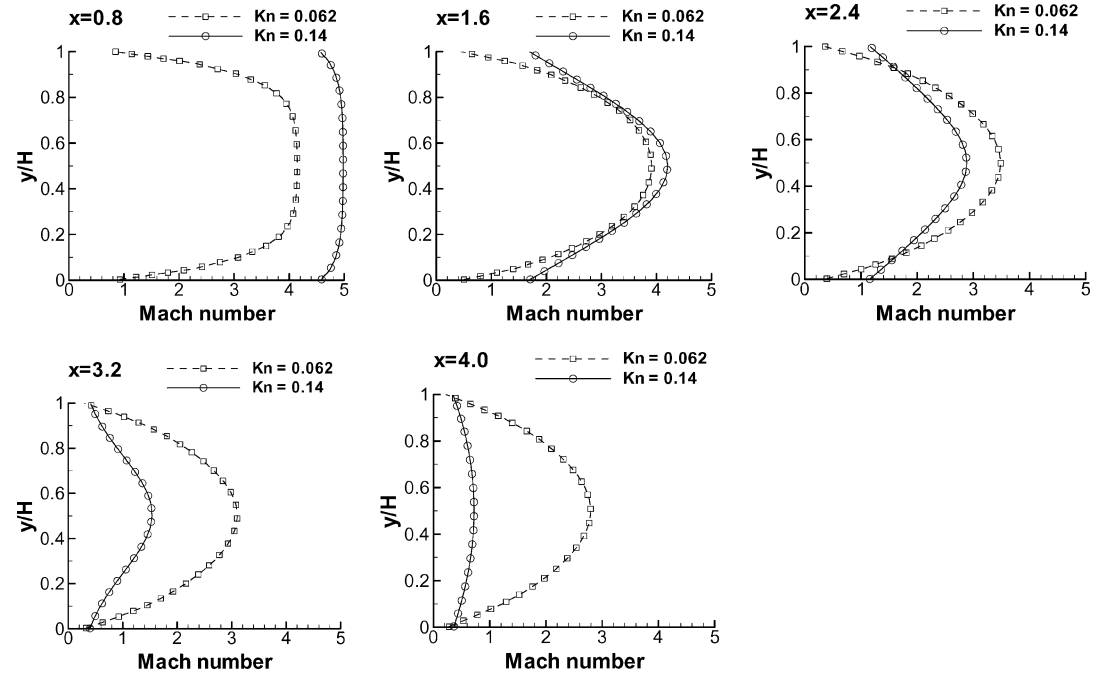

Fig. 13 Mach-number comparison along the *y* direction for various streamwise cross sections along the channel for $Kn = 0.062$ and 0.14.

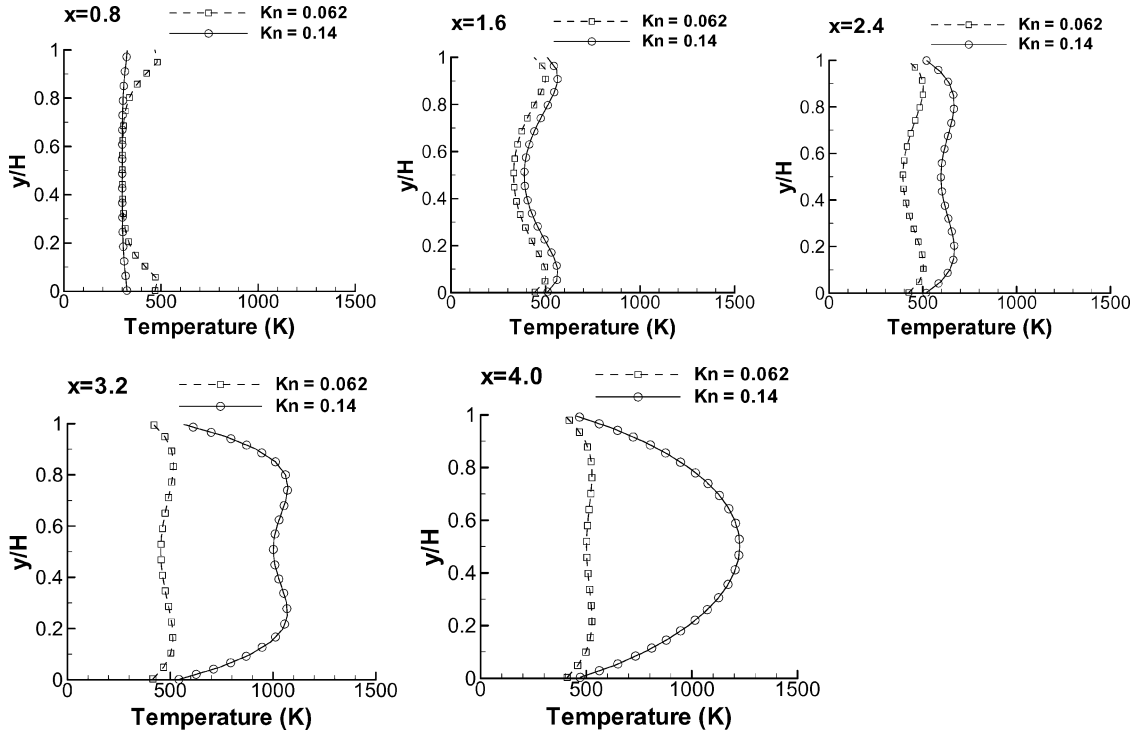

Fig. 14 Comparison of temperature solution along the *y* direction for various streamwise cross sections along the channel for *Kn* = 0.062 and 0.14.

reflected on the walls; the profile tends to become more parabolic near the downstream region as is seen for $x/H = 4.0$. The difference in the profile as seen for $x/H = 2.4$, and $x/H = 3.2$ reflects the effect of Knudsen number that increases along the length of the channel. Note that this disparity could be due to neglecting of the nonequilibrium effects.[28]

Figure 13 shows the distribution of the Mach number for various crosswise sections taken along the length of the microchannel for $x/H = 0.8$, 1.6, 2.4, 3.2, and 4.0. For $Kn = 0.14$ at $x/H = 0.8$, the flow is in the freestream region, and hence the profile is linear. This becomes parabolic for $x/H = 1.6$, and as the flow progresses downstream of the Mach-number profile the peak value decreases corresponding to the drop in velocity downstream. On the other hand, very small change in the parabolic profile for $Kn = 0.062$ is noticeable in the downstream region. Evidently, a higher Mach number produces more slip on the walls.

Corresponding sections for the temperature distribution show the development of thermal boundary layer. Figure 14 depicts these crosswise profiles of the temperature. In the freestream region the temperature remains linear. For $Kn = 0.14$, thermal boundary formation starts at $x/H = 0.8$ with knees near the top and bottom surfaces. This distortion merges towards the center of the channel as the flow develops. Finally at $x/H = 4.0$ the flow becomes fully developed with both peaks vanishing. For $Kn = 0.062$, the development of the thermal boundary does not complete at $x/H = 4.0$. The contours in Fig. 7a show that the boundary formation continues beyond $x/H = 4.2$.

Conclusions

A two-dimensional finite element based hydrodynamic model with the first-order slip/jump boundary conditions has been utilized to simulate high-speed gas flows and heat-transfer processes through short microchannels. The two cases considered incorporate different working fluids, namely, helium and nitrogen. The higher-Knudsen-number case with helium reflects higher heat-transfer characteristics. The heat-transfer characteristics predicted by the hydrodynamic model for this microchannel compared favorably with the reported direct-simulation Monte Carlo results. The deviation in values could possibly be caused by a difference in location where the exit backpressure was specified. It is important to note the variation of the Knudsen number along the flow, which can cause the solution discrepancy as Kundsen number increases downstream. Also the molecular viscosity of the working fluids varies as the temperature changes. The constant viscosity assumption thus limits the solution accuracy. For hypersonic flows one should investigate the effects of vibrational, rotational, and translational energy transfer mechanisms.[28] Further size reduction of the transport carrier can result in incorrect modeling of the shear stress and nonequilibrium processes. In such a case one can significantly alter predicted flow properties by controlling the nature of the pore surfaces[21] and possibly by modifying the bulk viscosity and adding the quantum effect.

References

[1]Karniadakis, G., and Beskok, A., *Micro Flows-Fundamentals and Simulation*, Springer-Verlag, New York, 2002.

[2]Schaaf, S. A., and Chambre, P. L., *Flow of Rarefied Gases*, Princeton Univ. Press, NJ, 1961.

[3]Maxwell, J. C., "On Stresses in Rarefied Gases Arising from Inequalities of Temperature," *Philosophical Transactions of the Royal Society Part 1*, Vol. 170, 1879, pp. 231–256.

[4]von Smoluchowski, M., "Ueber Wärmeleitung in Verdünnten Gasen," *Annalen der Physik und Chemi*, Vol. 64, 1898, pp. 101–130.

[5]Oran, E. S., Oh, C. K., and Cybyk, B. Z., "Direct Simulation Monte Carlo: Recent Advances and Applications," *Annual Review of Fluid Mechanics*, Vol. 30, 1998, pp. 403–441.

[6]Wu, P. Y., and Little, W. A., "Measurement of the Heat Transfer Characteristics of Gas Flow in Fine Channel Heat Exchanger Used for Microminiature Refrigerators," Cryogenics, Vol. 24, 1984, pp. 415–423.

[7]Pfahler, J., Bau, H., and Zemel, J. N., "Liquid Transport in Micron and Submicron Channels," *Sensors and Actuators*, Vol. A21–23, 1990, pp. 431–434.

[8]Choi, S. B., Barron, R. F., and Warrington, "Fluid Flow and Heat Transfer in Microtubes," *Proceedings of the ASME*, DSC, Vol. 32, 1991, pp. 123–134.

[9]Peng, X. F, Wang, B. X., Peterson, G. P., and Ma, H. B., "Experimental Investigation of Heat Transfer in Flat Plates with Rectangular Microchannels," *International Journal of Heat and Mass Transfer*, Vol. 38, No. 1, 1995, pp. 127–137.

[10]Adams, T. M., Ghiaasiann, S. M., and Abdel-Khalik, S. I., "Enhancement of Liquid Forced Convection Heat Transfer in Microchannels due to the Release of Dissolved Noncondensables," *International Journal of Heat and Mass Transfer*, Vol. 42, 1999, pp. 3563–3573.

[11]Mala, G. M, Li, D., and Dale, J. D., "Heat Transfer and Fluid Flow in Microchannels," *International Journal of Heat and Mass Transfer*, Vol. 40, 1997, pp. 3079–3088.

[12]Bird, G. A., *Molecular Gas Dynamics and the Direct Simulation of Gas Flows*, Oxford, England, UK, 1994.

[13]Xue, H., Ji, H. M., and Shu, C., "Analysis of Micro-Couette Flow Using the Burnett Equations," *International Journal of Heat and Mass Tansfer*, Vol. 44, 2001, pp. 4139–4146.

[14]Agarwal, R. K., Yun, K. Y., and Balakrishnan, R., "Beyond Navier–Stokes: Burnett Equations for Flows in Continuum-Transition Regime," *Physics of Fluids*, Vol. 13, No. 10, 2001, pp. 3061–3085.

[15]Oh, C. K., Oran, E. S., and Sinkovits, R. S., "Computations of High Speed, High Knudsen Number Microchannel Flows," *Journal of Thermophysics and Heat Transfer*, Vol. 11, 1997, p. 497.

[16]Liou, W. W., and Fang, Y., "Heat Transfer in Microchannel Devices Using DSMC," *Journal of Microelectromechanical Systems*, Vol. 10, No. 2, 2001, pp. 274–279.

[17]Mavriplis, C., Ahn, J. C., and Goulard, R., "Heat Transfer and Flowfields in Short Microchannels Using Direct Simulation Monte Carlo," *Journal of Thermophysics and Heat Transfer*, Vol. 11, No. 4, 1997, pp. 489–496.

[18]Gad-ek-hak, M., "The Fluid Mechanics of Microdevices—The Freeman Scholar Lecture," *Journal of Fluids Engineering*, Vol. 121, 1999, pp. 5–33.

[19]Raju, R., and Roy, S., "Hydrodynamic Model for Microscale Flows in a Channel with Two 90° Bends," *Journal of Fluids Engineering*, Vol. 126, No. 3, 2004, pp. 489–492.

[20]Roy, S., Raju, R., Chuang, H., Cruden, B., and Meyyappan, M., "Modeling Gas Flow Through Microchannels and Nanopores," *Journal of Applied Physics*, Vol. 93, No. 8, 2003, pp. 4870–4879.

[21]Cooper, S. M., Cruden, B., Meyyappan, M., Raju, R., and Roy, S., "Gas Transport Characteristics Through a Carbon Nanotubule," *Nano Letters*, Vol. 4, No. 2, 2004, pp. 377–381.

[22]Pong, K. C., Ho, C., Liu, J., and Tai, Y., "Non-Linear Pressure Distribution in Uniform Microchannels," *Application of Microfabrication to Fluid Mechanics*, FED, Vol. 197, 1994, pp. 51–56.

[23]Chen, C. S., Lee, S. M., and Sheu, J. D., "Numerical Analysis of Gas Flow in Microchannels," *Numerical Heat Transfer, Part A*, Vol. 33, 1998, pp. 749–762.

[24]Sreekanth, A. K., "Slip Flow Through Long Circular Tubes," *Rarefied Gas Dynamics*, edited by L. Trilling, and H. Y. Wachman, Vol. 1, Academic Press, New York, 1969, pp. 667–680.

[25]Piekos, E., and Breuer, K., "DSMC Modeling of Microchannel Devices," AIAA Paper 95-2089, 1995.

[26]Bhatia, S. K., and Nicholson, D., "Hydrodynamic Origin of Diffusion in Nanopores," *Physical Review Letters*, Vol. 90, 2003.

[27]Roy, S., and Cruden, B., "Hydrodynamic Modeling for Micro and Nanoscale Gas Flows," AIAA Paper 2004-2673, 2004.

[28]Josyula, E., Bailey, W. F., and Ku, K., "Nonequilibrium Relaxation in High Speed Flows," AIAA Paper 2004-2468, 2004.